Fourier magnetic imaging with nanoscale resolution and compressed sensing speed-up using electronic spins in diamond

K. Arai*, C. Belthangady*, H. Zhang*, N. Bar-Gill, S. J. DeVience,
P. Cappellaro, A. Yacoby and R. L. Walsworth.

* These authors contributed equally to this work.

I. Fourier magnetic microscope

The Fourier magnetic microscope consists of a home-built scanning confocal microscope and a diamond coverslip on which gradient microcoils were photo-lithographically defined. Optical excitation for the confocal microscope is provided by a 400 mW diode-pumped solid state laser (Changchun New Industries) operating at 532 nm. An 80 MHz acousto-optic modulator (Isomet Corporation) controls laser pulses for spin initialization and read-out. A single-mode fiber is used to clean up the mode profile of the laser and the output of the fiber is sent to a 100X oil-immersion objective with a numerical aperture of 1.3 (Nikon CFI Plan Fluor). The NV-containing diamond sample is mounted on a three-axis motorized stage (Micos GmbH) that allows scanning of the sample in the focal plane of the objective. Fluorescence from NV centres is separated from the 532 nm excitation light with a dichroic beam-splitter (Semrock LM01-552-25). After filtering through a long-pass filter (Semrock LP02-633RS-25), the fluorescence is focused into a single-mode fiber with a mode-field-diameter ~5 μm (which acts as the pinhole of the confocal microscope) and sent to a single-photon counting module (Perkin Elmer SPCM-ARQH-12). Pulses from the detector are read using the counter input of a DAQ card connected to a computer. Microwave excitation is provided by a signal generator (Agilent E4428C) whose output is amplified (Mini-circuits ZHL-16W-43-S+) and sent though a microwave loop defined on the diamond coverslip. Fabrication of the photo-lithographic patterns on the diamond coverslip is described in the Methods section of the main text. Gradient pulses are defined using the arbitrary waveform function of a programmable signal generator (Stanford Research Systems SRS345) and amplified by an audio-frequency amplifier (Texas Instruments LM4780). The bandwidth of the gradient pulses is limited by the slew rate of the amplifier to approximately 1 MHz.

II. Thermal effects of gradient microcoil operation

Supplementary Figure 1 shows how the gradient microcoil is integrated into the Fourier magnetic imaging microscope. UV-curing optical adhesives are used to glue the NV-diamond detector to the gradient microcoil. As specified in the Methods section, the

microcoil is fabricated on the front surface of a poly-crystalline diamond substrate for optimum heat dissipation. The back surface of this diamond substrate is attached to a copper heat sink cooled by an air fan to further remove heat. The resistance of each gradient microcoil is 1.4 Ω, such that 1.4 W of heat is generated at a typical peak current of 1 A. To assess thermal performance under standard operating conditions, the system was modeled using COMSOL Multiphysics software. With a heat sink and fan cooling we estimate a steady-state temperature rise of the diamond sample of <10 K at 1 A peak current. An analytical model based on techniques described in Ref. S1 gave similar temperature estimates.
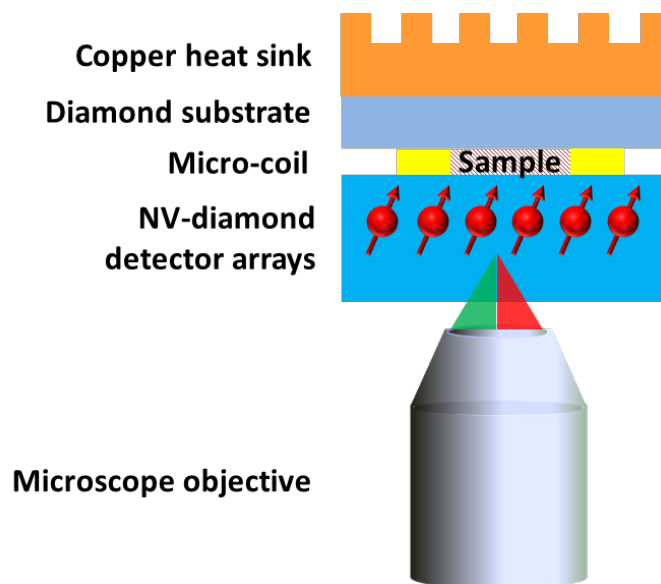
Supplementary Figure 1 | Schematic of Fourier magnetic imaging microscope. The gradient microcoil is placed close to a shallow NV layer (~20 nm from the diamond surface) and UV-curing optical adhesive is applied between the microcoil and the NV-diamond chip to form physical and thermal contact. A sample to be magnetically imaged could be inserted between the NV-diamond surface and microcoil. A poly-crystalline diamond chip is used as the microcoil fabrication substrate for optimum heat dissipation. Furthermore, the diamond substrate is thermally attached to a copper heat sink under the condition of extra air flow.

The rise in temperature was experimentally determined using two techniques. In the first technique, electron spin resonance (ESR) measurements were performed on NV centres within a nanopillar, both with and without a steady current of 1 A in the gradient microcoil (the maximum current used in Fourier imaging experiments). The magnetic field produced by the gradient microcoil induced a Zeeman shift of the ESR resonance line (in addition to that caused by the static magnetic field). A temperature change of the NV-diamond sample due to current in the gradient microcoil also caused a decrease in the zero-field splitting of 74.2 kHz per degree rise in temperature (Ref. S2). From the observed 1 MHz shift in the zero-field splitting when a steady current of 1 A was sent

though the microcoils, the temperature shift was estimated to be ≈13 K (Supplementary Fig. 2a). In the second experimental technique, the change in resistance of the gold microcoil was measured as a function of current. From the known value of the temperature coefficient of resistance of gold, the temperature rise at 1 A current was again estimated to be ≈13 K (Supplementary Fig. 2b). Note that the steady-state temperature rise of the integrated experimental assembly (NV-diamond sensor chip, microcoil, etc.) during Fourier magnetic imaging is estimated to be ≈5 K due to the finite duty cycle of the gradient pulse sequence, as shown in Fig. 1d of the main text, and the variable gradient strengths employed (mostly less than from the maximum 1 A current).
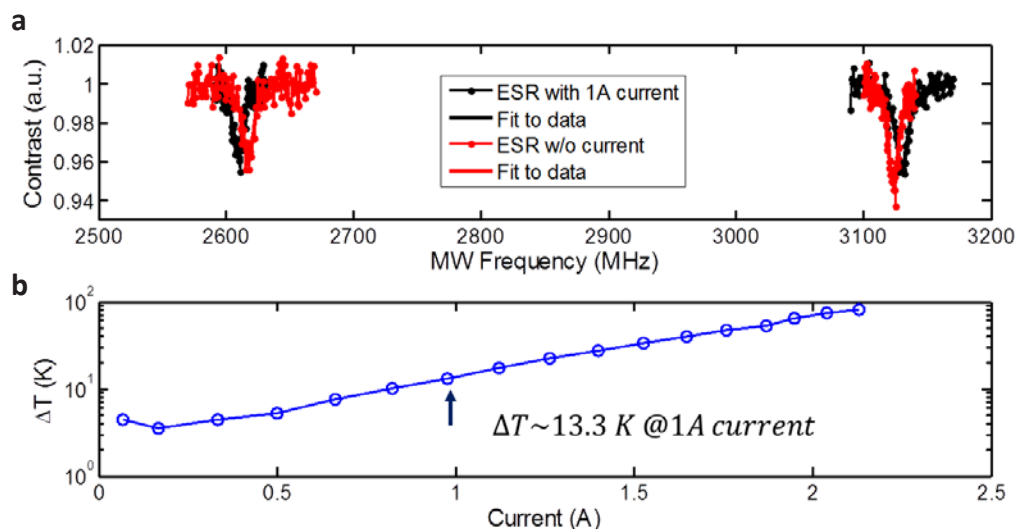
Supplementary Figure 2 | Measurements of the NV-diamond sensor's temperature change due to steady current through the gradient microcoil. **(a)** NV ESR spectral line shifts for 1 A current. The NV axial zero-field splitting parameter D varies with temperature T. By measuring the shift in D (midway between the $|0\rangle$ to $|\pm 1\rangle$ ESR frequencies), magnetic-field-induced (Zeeman) ESR line shifts can be removed and the diamond temperature change can be estimated. **(b)** Measurement of microcoil resistance change with increasing current. Here, the temperature coefficient of resistance for gold ≈0.0034 K^{-1} is used. When 1 A current is applied, the estimated temperature increase ≈13 K, consistent with the result from ESR measurements.

The above measurements were performed to characterize steady-state temperature rise during maximum activation of the gradient microcoils. To assess dynamic thermal effects during application of pulsed magnetic field gradients, the analytical formula listed in Ref. S1 was applied to estimate the microcoil's thermal time constant: $\tau_{fast} = C_W h/(k - hj^2\alpha\rho)$, where C_W is the heat capacity (per volume) of the microcoil, ρ is the microcoil's (cold) resistivity with a linearly approximated temperature coefficient α, h is the microcoil thickness, and j is the applied current density. For typical experimental conditions, this yields $\tau_{fast} \sim 0.25$ µs, which is an order of magnitude shorter than the

gradient switching period (~1 μs). The microcoil's thermal behavior is thus determined to be close to quasi-static during the gradient switching process, with insignificant effect from thermal shock. In addition, during a complete Fourier imaging experiment there is slow heating (related to heat dissipation within the substrate and heat sink) that was measured to be on the order of seconds, which is much slower than the gradient "on time" for phase-encoding (~100 μs NV interrogation time). Thus the gradient strength is stable during each k-space measurement and the overall system temperature increase during data acquisition (5 K, as noted above) is stable to ~1 K after the initial few-second transient. In all, the thermal performance of the system was found to be well understood, with insignificant corruption of the Fourier imaging results.

III. Gradient calibration

As described in the main text, NV signals for a point in k-space have the form $s(\vec{k}) \sim \cos(2\pi\vec{k}.\vec{r}_0)$, where $\vec{k} = (2\pi)^{-1}\gamma\tau(dB_\zeta/dx, dB_\zeta/dy)$. Thus the magnitude of k is proportional to the magnetic field gradient, which is in turn proportional to the current I, and this current is proportional to the voltage V applied by the SRS345 programmable signal generator. The overall proportionality constant, which maps V to k, was estimated using the procedure described below.

A low-resolution one-dimensional phase encoding sequence was run sequentially on a set of 7 nanopillars along the X (and separately Y) direction. The NV signal was measured as a function of SRS345 voltage, V. The signal for each nanopillar was then Fourier transformed to obtain a peak in "inverse voltage" space. The peak positions (in units of Volt^{-1}) were then plotted as a function of nanopillar positions. The inter-pillar spacing of 1 micron, known from the defined lithographic pattern (see Methods), allowed conversion between Volt^{-1} units and distance units in microns. This calibration procedure made accurate determination of local gradients possible and also properly accounted for any misalignment between the diamond coverslip patterned with microcoils and the NV-containing diamond sample. Calibration data for the Y micocoils is shown in Supplementary Fig. 3 below. Similar results were obtained for the X coils. In the previous section, systematic effects due to heating are discussed. Another potential source of systematic error in the gradient calibration is the variation of NV centre positions in the nanopillars. If the NV centres are assumed to be randomly distributed in a nanopillar, then the root-mean-square deviation of NV position of a given crystallographic orientation, projected onto the X axis from the center of the nanopillar, is 140 nm, for the measured NV density in the sample. Since 7 nanopillars are used for this gradient calibration, the total spacing between the leftmost and rightmost pillars is 6000 nm. The estimated error of the magnetic field gradient field is thus 140 nm/6000 nm/√7 = 0.9%. The factor of √7 is included because there are 7 data points (i.e., nanopillars) with uncorrelated variations in NV positions. The additional uncertainty introduced to the Fourier imaging resolution by this method of gradient calibration is 0.04 nm for 1-d imaging and 0.3 nm for 2-d imaging. To further reduce this uncertainty in future work, the gradient calibration could be extended to include additional rows of nanopillars.

Gradient Calibration Curve
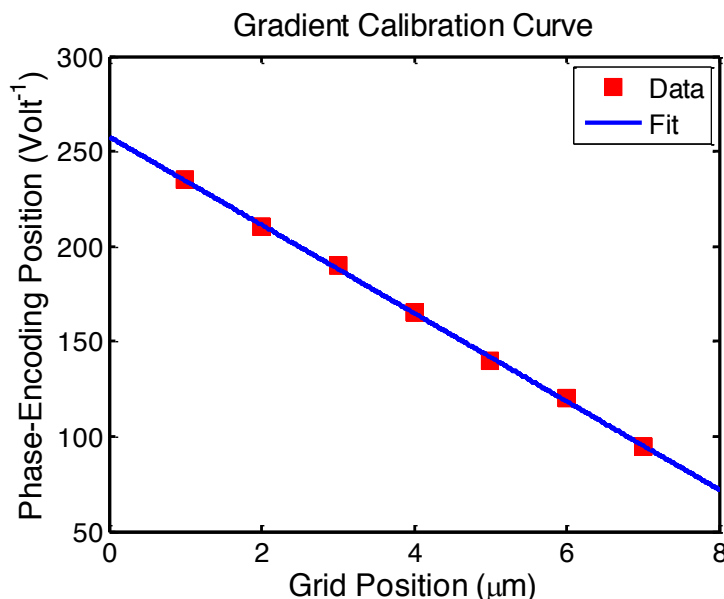
Supplementary Figure 3 | 1D low resolution phase encoding measurements for the Y micocoil gradient calibration. The slope of the blue line is -23 V^{-1}/μm. The SRS345 voltage is divided by this value to obtain k-space data in μm^{-1} units.


IV. Magnetic field estimates and measured values for wide FOV image

For the three example nanopillar magnetic images shown in Fig. 4 of the main text, the AC magnetic field differences between NV centre pairs, as determined from Fourier magnetic imaging, are $\Delta B_{J=1} = [6.5 \pm 1.1] \times 10^2$ nT, $\Delta B_{J=2} = [1.9 \pm 0.6] \times 10^2$ nT, and $\Delta B_{J=3} = [0.8 \pm 0.4] \times 10^2$ nT. A measure of the long-range magnetic field gradient is provided by the low-resolution real-space image: $\vec{\nabla} B(\vec{r}_J) = [(B(x_{J+1}) - B(x_J))/\Delta x,$ $(B(y_{J+1}) - B(y_J))/\Delta y]$, where $B(\vec{r}_J)$ is the spatially-averaged magnetic field magnitude at the Jth nanopillar located at position $\vec{r}_J = [x_J, y_J]$, and $\Delta x, \Delta y = 1$ μm is the distance between adjacent nanopillars. The expected magnetic field difference between NV centres within the Jth nanopillar is then given by: $\Delta B^{exp}(\vec{r}_J) = \vec{\nabla} B(\vec{r}_J) \cdot (\vec{r}_l - \vec{r}_m)$, where $\vec{r}_l, \vec{r}_m$ are the NV positions determined via Fourier imaging. For $J = 1$, for example, the local gradient is $(B(x_{J+1}) - B(x_J))/\Delta x = (32.2 - 29.7)$ μT/1 μm $= 2.5$ μT/μm , $(B(y_{J+1}) - B(y_J))/\Delta y = (35.7 - 29.7)$ μT/1 μm $= 6.0$ μT/μm, and the NV separation is $x_l - x_m = 90$ nm, $y_l - y_m = 60$ nm . The expected magnetic field differences between NVs in the three example nanopillars are thus: $\Delta B^{exp}_{J=1} = [5.9 \pm 1.4] \times 10^2$ nT, $\Delta B^{exp}_{J=2} = [2.0 \pm 1.1] \times 10^2$ nT, and $\Delta B^{exp}_{J=3} = [1.5 \pm 0.6] \times 10^2$ nT, which are in close agreement with the Fourier-measured values.

V. Noise statistics and thresholding

The noise in k-space signals was observed to be Gaussian in nature. Upon Fourier transformation, the noise in the real and imaginary parts of the real-space signal was also observed to be Gaussian, as shown in Supplementary Fig. 4. This is to be expected, as

Fourier transformation is a linear operation and will not alter noise statistics. The noise in the absolute value of the real-space signal, however, was observed to follow a Rayleigh distribution (Supplementary Fig. 4c). This is well known in the theory of MRI (Ref. S3). The standard deviation of the Rayleigh distribution was computed and the real-space data was thresholded at 5 times this standard deviation to obtain the 2D images of NV centres shown in the main text. In the 2D imaging experiment in Fig 2e, the total free precession time was $\tau = 30$ μs. For each point in k-space, the sequence was repeated 30,000 times to improve the signal-to-noise ratio. The image was acquired for k_x and k_y values between -0.018 nm^{-1} and +0.018 nm^{-1} in 64 x 64 steps. The 2D imaging experiment was then repeated 21 times to further improve the signal-to-noise ratio, such that the total data acquisition time per k value was 25.2 seconds. Plotted in Fig. 2f is the amplitude of the Fourier-transformed signal ($abs[S(\vec{r})]$).
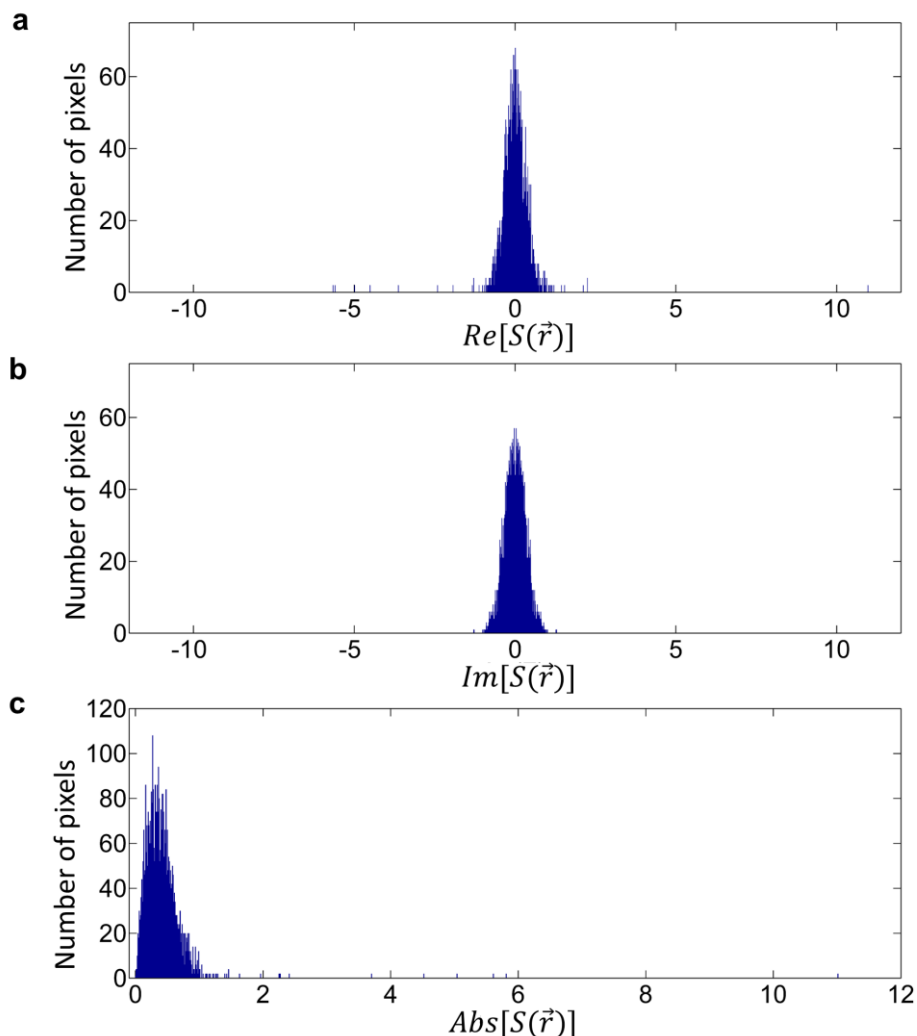
Supplementary Figure 4 | Analysis of noise statistics. Fourier transform of k-space data from Fig. 2e of the main text. **(a)** Histogram of the real part of the Fourier transformed real-space signal. **(b)** Histogram of the imaginary part of the Fourier transformed real-space signal. The data of (a) and (b) exhibit Gaussian noise; and are fit to extract the

standard deviation, σ of the noise. **(c)** Histogram of the absolute value of the Fourier transformed real-space signal. The noise follows a Rayleigh distribution.

VI. Multiplex advantage

This section discusses the circumstances under which Fourier (k-space) imaging is faster than imaging based on point-by-point (real space) scanning. To make the discussion broad-based and not specific to NV centres, the following simplifying assumptions are made: (i) there are N_E ideal photon emitters that emit R photons per second, which are to be imaged using both point-by-point scanning and Fourier techniques; and (ii) each emitter is a two-level spin system with optical contrast =1, i.e., all R photons are emitted by the spin-down state and zero photons by the spin-up state.

For the case of point-by-point scanning, if the imaging device scans over N_{pix} number of pixels spending time dt per pixel, then the total imaging time is $N_{pix}dt$ and the SNR is $\sqrt{Rdt}$. The data acquisition time, defined as $T_{SNR=1} = T/\text{SNR}^2$, where T is the total data acquisition time per k-value, is therefore given by $T_{SNR=1} = 1/R$.

In Fourier imaging, data is first acquired in k-space. Assuming the number of k-space points is N_{pix} and photons are counted for time dt per pixel, the total imaging time is $N_{pix}dt$ and the SNR in k-space is $\sqrt{N_E Rdt}$. To compute SNR in real space (i.e., after Fourier transformation), Parseval's theorem yields $(Signal)_r = N_{pix}/\sqrt{N_E}(Signal)_k$ and $(Noise)_r = \sqrt{N_{pix}}(Noise)_k$, which implies $(\text{SNR})_r = \sqrt{N_{pix}/N_E}(\text{SNR})_k$. Here the subscripts r and k represent real space and k-space respectively. The SNR for Fourier imaging is therefore equal to $\sqrt{N_{pix}Rdt}$, which is higher than the SNR for point-by-point scanning by a factor $\sqrt{N_{pix}}$. Consequently, the total data acquisition time for Fourier imaging is $T_{SNR=1} = 1/(R * N_{pix})$, which is less than that of point-by-point scanning by a factor N_{pix}. This improvement in SNR (or equivalently, multiplex speed-up in data acquisition time) is well known in FTIR spectroscopy, where it is referred to as the Fellgett advantage [S4].

In Supplementary Fig. 5 data from Figs. 2a and 2b of the main text is used to show how SNR in real space scales with the number of pixels under our experimental conditions. The SNR is observed to increase with the number of pixels albeit with a slightly smaller exponent of 0.36(8) instead of 0.5. The distribution of the noise in the presence of phase encoding signal is Rician, which is a convolution between Gaussian and Rayleigh. For a signal-to-noise ratio (SNR) < 2, this noise is well approximated by a Rayleigh distribution. Thus, the measured SNR in this regime appears larger than that expected from a pure Gaussian. If this biasing effect, which could apply to the first two data points (where $N_{pix} \sim 128, 256$), is taken into account, the exponent may approach 0.5. It is also noted that the full multiplex enhancement in SNR may not always be realized under realistic experimental conditions. For example, if the optical contrast is not perfect or if the point-spread-function of the signal peaks is wider than the imaging resolution, then the multiplex advantage will be diminished, though it may still be substantial. These issues will be addressed more in detail in future work.
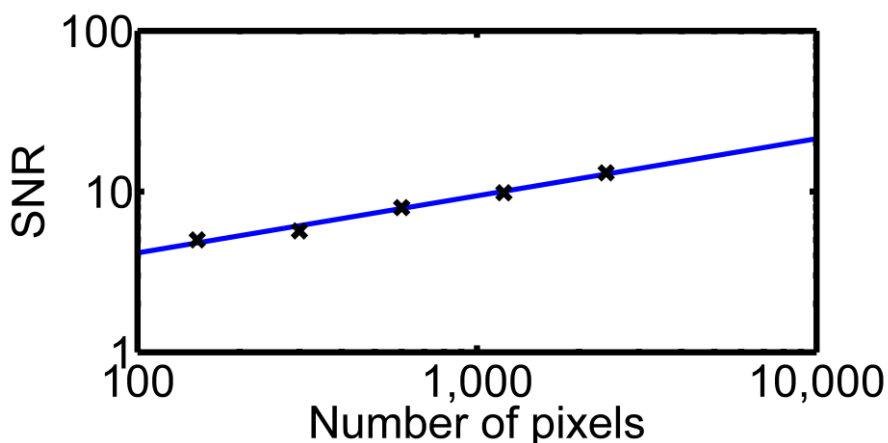
Supplementary Figure 5 | Scaling of SNR with number of number of pixels. Fit to data (blue line) shows SNR scales as $N_{pix}^{0.36(0.8)}$ which is close to but smaller than the expected $N_{pix}^{0.5}$ scaling.

VII. Magnetic field and gradient sensitivity

The magnetic field sensitivity and the field gradient sensitivity are calculated from the data presented in Fig. 3. In this measurement, information about NV centre location and its local magnetic field is phase-encoded in 128 pixels, with a pulse sequence length of 20 μs for each data point in k-space. This Fourier magnetic imaging protocol is then repeated 3×10^5 times to improve the signal-to-noise ratio. The total data acquisition time is therefore $T_{tot} = 768$ sec. The magnetic field sensitivity is given by η = $\sigma\sqrt{T_{tot}}/(dS/dB)$, where σ is the noise, and dS/dB is the slope of the magnetometry curve. From the low-resolution magnetic field measurement in Fig. 4, the current-to-field conversion is found to be dB/dI = 0.0058 Tesla/Ampere. From Fig. 3c, one can determine σ = 0.11, dS/dI = $2\pi * 2.3 * 10^3$ A^{-1}. The magnetic field field sensitivity is therefore η = $1.2 * 10^3$ nT/$\sqrt{Hz}$.

The gradient sensitivity between the two NV centres in Fig. 3 of the main text is calculated from the uncertainty of the field gradient, which is given by G = $\Delta B/\Delta x$, where $\Delta B = B(x_1) - B(x_2) = 650$ nT is the measured field difference between the two NV centres and $\Delta x = x_1 - x_2 = 121$ nm is the distance between them. Through error propagation the minimum detectable gradient is found to be $\delta G = G [(\delta\Delta B/ \Delta B)^2 + (\delta\Delta x/\Delta x)^2]^{1/2}$ where $\delta\Delta B = \sqrt{2} * \delta B = \sqrt{2}*(1200$ nT/$\sqrt{Hz}$ /$\sqrt{768}$sec) = 61 nT is the uncertainty in the magnetic field difference, and $\delta\Delta x = \sqrt{2} * \delta x \sim \sqrt{2}$ (30nm /SNR/$\sqrt{T_{tot}}$) is the uncertainty in the NV separation. Note that the dominant contribution comes from the first term, but that all errors are relatively small, justifying the error propagation analysis. The magnetic field gradient sensitivity is thus given by $\eta_G = \delta G\sqrt{T_{tot}} \approx (650$ nT/121nm)(61 nT/650 nT)*$\sqrt{768}$sec = 14 nT/nm/$\sqrt{Hz}$.

VIII. Nanopillar map
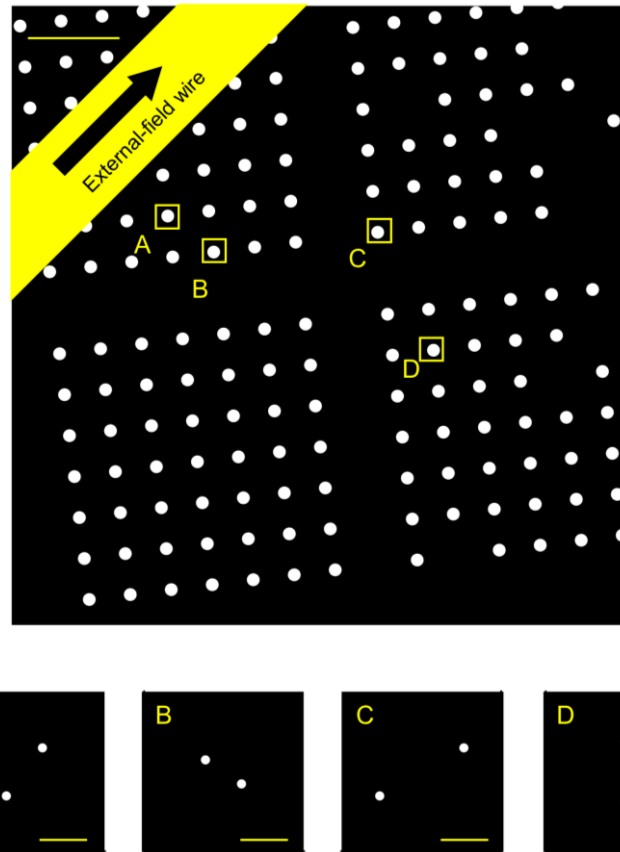
Supplementary Figure 6 | Location of nanopillars relative to the external-field wire. Data for Figs. 2c-f and Fig. 3 of the main text were taken from nanopillar B. Data for Fig. 4 of the main text was taken from nanopillars B, C, and D. The compressed sensing data of Fig. 5 of the main text was taken from nanopillar A. Scale bars are 2 μm and 100 nm for top and bottom figures, respectively.

IX. Wide applicability of Fourier magnetic imaging technique

NV Fourier magnetic imaging, which employs phase-encoding of the detector NV spins rather than of the sample spins as in previous Fourier techniques, should be applicable to a broad range of systems that can be placed on or near the diamond surface. With the microcoil design and experimental conditions implemented in the present work, the maximum magnetic field difference generated by the gradients is ±5 G across the largest field of view; and the gradient switching time is slower than 1 μs. Within these operating conditions, a wide range of nano-magnetic systems of interest will be unperturbed by such pulsed magnetic field gradients. See Supplementary Table 1 and Supplementary Fig. 7.

Physical phenomena of interests	Minimum magnetic field to perturb system, H_{min} (Oe)	Time scale	System (materials)	Reference
Magnetic vortex core reversal	15	4 ns	$Ni_{80}Fe_{20}$	S11
	800	100 ps	$Ni_{81}Fe_{19}$	S12
	~1000	static	$Ni_{80}Fe_{20}$	S13
Ferromagnetic resonance (FMR)	~1000	static	$Ni_{80}Fe_{20}$	S14
Domain wall (DW) motion	~15	static	YIG	S15
	~ 50	static	Co/Ni	S16
	~ 500	~ 5 ns	$Ni_{80}Fe_{20}$	S17
Skyrmion	~100	static	Cu_2OSeO_3	S18
	~1000	static	FeGe	S18

Supplementary Table 1 | A survey of the minimum external magnetic field (H) required to perturb several condensed matter nano-magnetic phenomena of current research interest, as well as the characteristic timescales of these phenomena. In air, an H-field of 1 Oe corresponds to a B-field of 1 Gauss. All of these systems would be unperturbed by the magnetic field gradients implemented with our NV-diamond Fourier magnetic imaging technique.
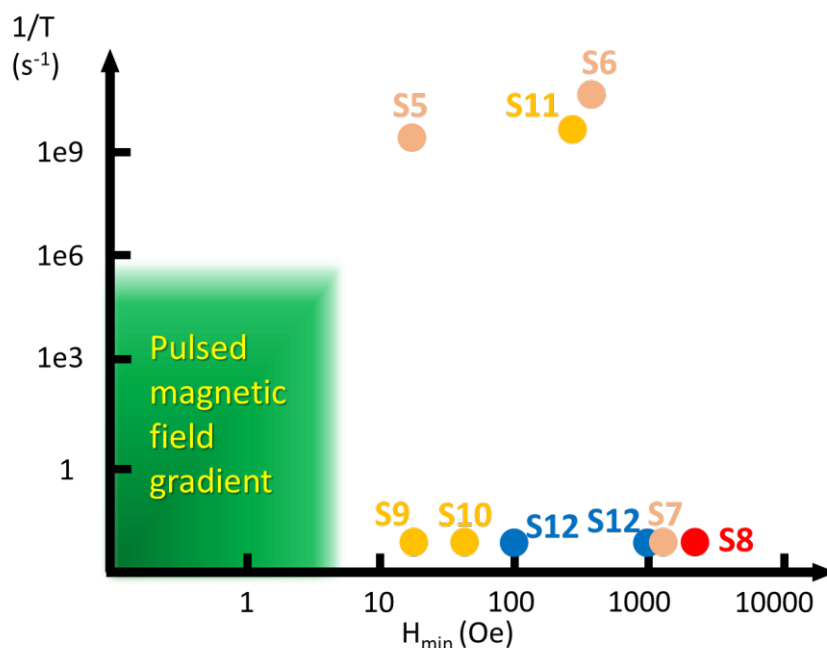
Supplementary Figure 7 | Scatter plot of the magnetic field strengths and switching rates required to perturb several example condensed matter systems. Colored dots represent systems listed in the Table above. Numbers correspond to the referenced literature. The green region indicates the working region of the pulsed magnetic field gradients implemented in our NV Fourier magnetic imaging demonstrations, which have a maximum magnetic field of ±5 G and fastest switching rate of 1 MHz.

References:

S1. Groth, S. et al., *Appl. Phys. Lett.* **85**, 2980 (2004).

S2. Acosta, V. M. *et al., Phys. Rev. Lett.* **104,** 070801 (2010).

S3. Gudbjartsson, H. et al., *Magn. Reson. Med.* **34**, 910 (1995).

S4. P. B. Fellgett *J. Phys. Radium* 19, 187 (1958).

S5. Van Waeyenberge, B., *et al*., *Nature* **444**, 461-464 (2006).

S6. Hertel, R., Gliga, S., Fahnle, M. & Schneider, C. M., *Phys. Rev. Lett*. **98**, 117201 (2007).

S7. Okuno, T., *et al*., *J. Magn. Magn. Mater*. **240**, 1-6 (2002).

S8. Lee, I., *et al*., *Nature* **466**, 845-848 (2010).

S9. Xia, W. X., *et al*., *J. Appl. Phys*. **108**, 123919 (2010).

S10. Koyama, T., *et al*., *Appl. Phys. Lett*. **98**, 192509 (2011).

S11. Kim, J.-S., *et al*., *Nature Commun*. **5**, 3429 (2014).

S12. Nagaowa, N. & Tokura, Y., *Nature Nanotech*. **8**, 899-911 (2013).